

# Constraint Handling in a Fuel Cell System: A Fast Reference Governor Approach

Ardalan Vahidi, Ilya Kolmanovsky, and Anna Stefanopoulou

**Abstract**—A compressor-based air supply system in a fuel cell is susceptible to saturation during fast transients in load. Aggressive control of the air compressor may result in compressor surge or choke, disrupt the flow of air into the cathode of a fuel cell stack, and negatively impact the fuel cell power generation. Low partial oxygen pressure in the cathode caused by rapid increase in load may also damage the stack and reduce its life. A load governor can be added to the air supply control system to monitor the load and prevent violation of constraints (compressor surge, choke, and partial oxygen pressure) by modifying the load command to the fuel cell system. In this paper, we present the steps involved in the design of such a load governor for the fuel cell application. To reduce the online computations, we utilize the “fast” reference governor (FRG) approach which has been developed for linear systems. FRG utilize a “maximal constraint admissible set” calculated offline and, thus, require fewer online calculations. We propose a modification to the FRG design to make it applicable to the nonlinear fuel cell plant. The scheme is then implemented on a real-time simulation platform and it is shown that the computations of the load governor can be performed in real-time.

**Index Terms**—Compressor surge, fast reference governor (FRG), fuel cell, load governor, oxygen starvation.

## I. INTRODUCTION

**I**N FUEL CELL powered vehicles, one of the performance bottlenecks is posed by the air supply system. In a high pressure proton exchange membrane (PEM) fuel cell, a compressor supplies air to the cathode. The compressor itself consumes up to 30% of fuel cell generated power and, therefore, its size has direct influence on overall system efficiency. More importantly the compressor performs the critical task of providing the oxidant into the stack. It is known in the fuel cell community that low partial oxygen pressure in the cathode reduces the fuel cell voltage and the generated power, and it can reduce the life of the stack [1]. The challenge is that oxygen reacts instantaneously as current (load) is drawn from the stack, while the air supply rate is limited by the manifold dynamics, compressor surge, and choke constraints [2],

[3]. Surge causes large variations in flow and sometimes flow reversal through the compressor. Large amplitude surge may even damage the compressor [4], [5]. Reference [6] develops an active surge control approach for centrifugal compressors. Choke happens at sonic mass flow and is an upper limit to the amount of air the compressor can provide. In the fuel cell system there is a potential for compressor choke during a step-up in current demand. In addition, there is a potential for compressor surge during a step-down in current demand. For instance, the air flow controller reduces the compressor motor voltage during a step-down in current demand. A sudden decrease in compressor motor voltage is followed by a fast decrease in the compressor rotational speed. Since the manifold pressure cannot drop as quickly, surge may occur.

Low-pass filtering of the current demand to a fuel cell during steps in current can prevent constraint violation. The design of these filters is usually conservative to ensure satisfactory operation under various operating conditions (see, e.g., [7]). The transients may be managed with a load governor which modifies the current drawn from the fuel cell by only as much as needed for constraint enforcement. In principal, the design of such a load governor is based on online constraint optimization.

Sun and Kolmanovsky [7] have developed a load governor for oxygen starvation prevention in a fuel cell using a nonlinear reference governor (RG) approach. The constraints of the compressor are not considered in their work. Their RG searches at each sample time instant for the optimal and constraint admissible current demand to the fuel cell based on online optimization of a scalar parameter and online simulations of a nonlinear fuel cell model. Their approach ensures robustness against parameter variations, but may be computationally demanding. To implement the load governor in memory- and chronometric-constrained automotive microcontrollers, it is desirable to reduce the online computational effort as well as RAM and ROM requirements.

Our goal in the present paper is to develop a computationally efficient load governor which enforces the compressor surge, compressor choke, and oxygen starvation constraints in a fuel cell system. We start by employing the fast reference governor (FRG) approach proposed in [8] for linear systems for reducing the size of the optimization problem and computational effort. To this end, we formulate a load governor for a linearized model of the fuel cell system. We then present modifications so that the load governor can be applied to the nonlinear fuel cell model. Furthermore, we demonstrate that the order of the load governor can be reduced without much sacrifice on the performance by using a reduced-order fuel cell model. Finally, we explain implementation of the load governor on a real-time simulation platform and discuss real-time computational requirements.

Manuscript received November 22, 2005. Manuscript received in final form July 18, 2006. Recommended by Associate Editor Y. Jin. The work of A. Vahidi was supported in part by the National Science Foundation under Grant 0201332 and through the Automotive Research Center under the U.S. Army under Contract DAAE07-98-3-0022.

A. Vahidi is with the Department of Mechanical Engineering, Clemson University, Clemson, SC 29634-0921 USA (e-mail: avahidi@clemson.edu).

I. Kolmanovsky is with Ford Research and Advanced Engineering Department, Ford Motor Company, Dearborn, MI 48124 USA (e-mail: ikolmano@ford.com).

A. Stefanopoulou is with the Walter E. Lay Auto Lab, University of Michigan, Ann Arbor, MI 48109 USA (e-mail: annastef@umich.edu).

Color versions of Figs. 1–17 are available online at <http://ieeexplore.ieee.org>.  
Digital Object Identifier 10.1109/TCST.2006.883242

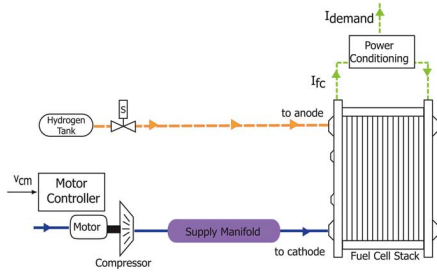


Fig. 1. Schematic of air supply control system.

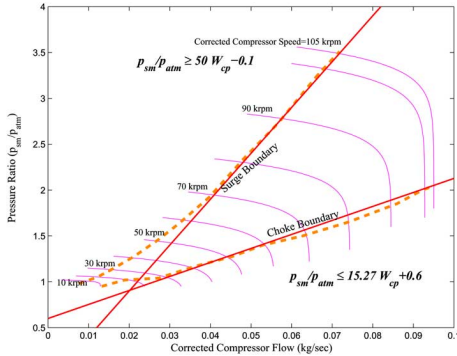


Fig. 2. Compressor map with approximated surge and choke boundaries.

## II. PROBLEM DESCRIPTION

Constraint management of the high pressure air supply system for a 75-kW PEM fuel cell with 350 cells is addressed in this paper. A schematic of the fuel cell system is shown in Fig. 1.

Hydrogen is supplied from a hydrogen tank and its flow is directly controlled by an inlet valve. A compressor supplies high pressure air to the cathode. The control input to the system is the compressor command  $v_{cm}$ , which influences the speed of the compressor and, consequently, the amount of air that is supplied to the cathode. The current taken from the fuel cell  $I_{fc}$  determines the rate at which hydrogen and oxygen are consumed, i.e., larger currents require more oxygen and hydrogen to be supplied. Given the current taken from the fuel cell  $I_{fc}$ , and the voltage supplied to the compressor motor  $v_{cm}$  (and also the ambient conditions), the state of species in the stack can be determined. In this paper, we will keep track of the compressor flow  $W_{cp}$  and the pressure downstream of the compressor  $p_{sm}$  since they, together, indicate if the compressor is near choke saturation or surge instability as shown in Fig. 2. The dashed lines shown in this compressor map represent boundaries beyond which compressor surge and choke can occur. Later, in this paper, we enforce pointwise-in-time constraints to ensure operation of the compressor inside the bounded region and away from the surge and choke regions.

As mentioned in the introduction, low oxygen concentration in the cathode (oxygen starvation) negatively affects the fuel cell voltage response and can even permanently damage the cells. A parameter called oxygen excess ratio  $\lambda_{O_2}$ , is defined as the ratio

between oxygen supplied and the oxygen reacted in the cathode. Low values of  $\lambda_{O_2}$  lead to oxygen starvation which should be strictly prohibited. Thus, a lower limit on  $\lambda_{O_2}$  is another constraint that we should enforce during operation of the fuel cell.

A phenomenological lumped parameter model of the fuel cell is used in this work to predict and prevent violation of the surge, choke, and starvation constraints. The fuel cell model used here is the nonlinear spatially-averaged model of the fuel cell stack together with its auxiliaries presented in [9] based on electrochemical, thermodynamic, and fluid flow principles. The stack model represents membrane hydration, anode and cathode flow, and stack voltage. This stack model is augmented with the models of ancillary subsystems including the compressor, manifold dynamics, cooling system, and the humidifier to obtain a nonlinear model of the overall fuel cell system. Since the focus of this paper is on the load governor, we just provide a summary of the model equations in the appendix of this paper; details of the model can be found in [9] and [10].

Due to the complexity of the model, all the governing equations cannot be easily shown in a concise closed form. However, the general state-space form is

$$\begin{aligned} \dot{x}_{nl} &= h(x_{nl}, v_{cm}, I_{fc}) \\ y_{nl} &= [W_{cp} \quad p_{sm} \quad \lambda_{O_2}] \end{aligned} \quad (1)$$

where the nine dynamic states in the model are shown in the equation at the bottom of the page, representing, respectively, oxygen mass in the cathode, hydrogen mass in the anode, nitrogen mass in the cathode, air compressor speed, supply manifold pressure, mass of air in the supply manifold, water mass in the anode, return manifold pressure, and water mass in the cathode. Three outputs of interest are compressor air flow  $W_{cp}$ , manifold pressure  $p_{sm}$ , and oxygen excess ratio  $\lambda_{O_2}$ .

Fig. 3 shows the nonlinear simulation results for the model during a series of step changes in current. During the current steps, the compressor motor input is calculated as a function of current drawn from the fuel cell based on a feedforward map. This feedforward map is designed such that at steady-state the oxygen excess ratio is regulated at the value of 2.<sup>1</sup> The Figure shows current, compressor input, compressor flow, manifold pressure, and oxygen excess ratio. It can be shown that while the compressor flow and manifold pressure increase when the current increases, an undesirable rapid drop in oxygen excess ratio still occurs during sudden changes in current levels.

Fig. 4 shows the evolution of the compressor flow<sup>2</sup> and pressure ratio in the compressor map during the transients of Fig. 3. During a step-up in  $v_{cm}$  command, the compressor flow increases faster than the pressure  $p_{sm}$  downstream from the compressor. As a result the compressor operates near the choke

<sup>1</sup>It is shown in [9] that oxygen stoichiometry of 200% ( $\lambda_{O_2} = 2$ ) results in maximum fuel cell net power. It also provides a good margin of safety against starvation.

<sup>2</sup>In all the compressor maps in this paper, the x-axis shows the corrected compressor flow. The steps for correcting the compressor flow are shown in Table IV in the appendix.

$$x_{nl} = [m_{O_2} \quad m_{H_2} \quad m_{N_2} \quad v_{cm} \quad p_{sm} \quad m_{sm} \quad m_{w,an} \quad p_{rm} \quad m_{w,ca}]^T$$

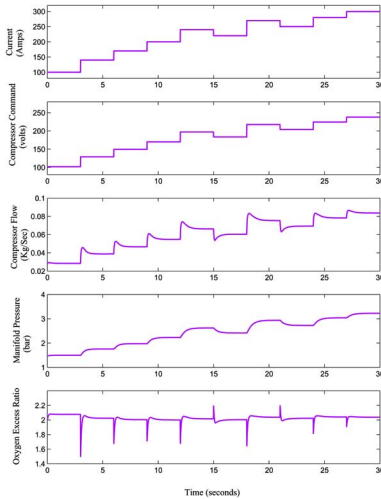


Fig. 3. Fuel cell model response to step changes in current demand.

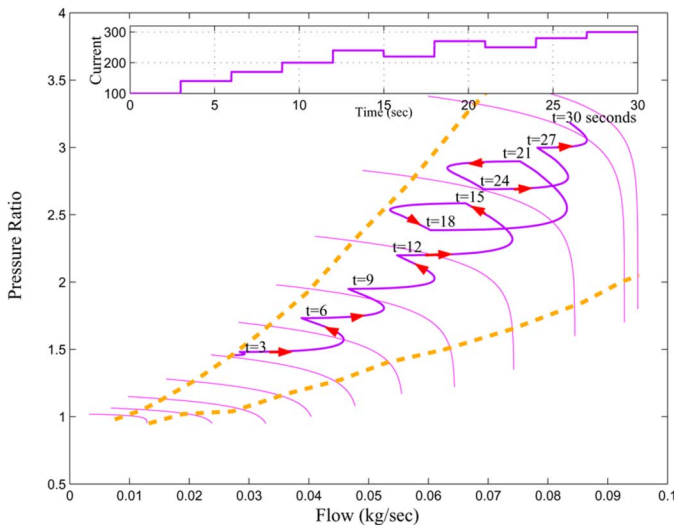


Fig. 4. Compressor response to step changes in current demand.

boundary. During a step-down in  $v_{cm}$ , the operating trajectory nears the surge boundary. Larger steps in the current require larger compressor commands that, if applied instantaneously, may result in surge or choke.

It can be shown from the previous results that rapid transients in current can send the compressor into surge or choke and saturate the air supply system or result in oxygen starvation in the cathode. However, once the compressor control system is designed to meet basic control design requirements (for example, closed-loop stability, overshoot, etc.) a load governor can be added for constraint enforcement. A load governor, shown in Fig. 5, is an add-on device that slows the transitions in current demand  $I_d$ , so that the constraints are not violated. A load governor, can be as simple as a first-order filter which is designed for the worst case current demand. The drawback of such a passive filter is that it slows down the system response even under small transients. The transients can be managed less conservatively with an active load governor which modifies the reference command only when needed to avoid constraint violation.

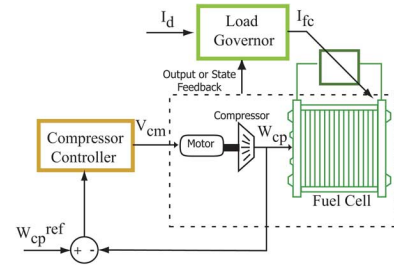


Fig. 5. Schematics of fuel cell air supply control.

Modification of the reference command to a close-loop control system for enforcing constraints has been studied under the more general title of RG. A good body of literature has been developed in the past fifteen years to establish theoretical properties of reference governors.

In principle, two different strategies have been used for design of RGs. One approach is based on the ideas of model predictive control. The problem is posed as an optimization problem, one in which the difference between the reference command and actual command is minimized over a future horizon, subject to pointwise-in-time constraints. Bemporad *et al.* [11] use this approach and formulate the RG in a quadratic programming framework. Bemporad [12] extends this receding horizon strategy to a nonlinear system and use a bisectional search approach to solve the optimization problem. Casalova and Mosca [13] address the robustness with the governor when a linear system is subject to bounded input disturbance.

The other strategy is based on characterizing a set of initial conditions and references that would satisfy the constraints. This idea of maximal output admissible sets has been developed by Gilbert and Tan [14] for design of error governors and further expanded by Gilbert and Kolmanovsky to design of RGs for linear [8] and nonlinear [15] systems. In [8], it is shown that for linear systems the RG can be constructed largely offline, while the online computational effort can be systematically reduced at the expense of the increased conservatism in the RG operation. Because of the reduced online computations, the governor is called a fast reference governor (FRG). Disturbances are addressed based on forming disturbance invariant sets [16].<sup>3</sup>

In this paper, we use the FRG approach introduced in [8] for the fuel cell problem.

### III. LOAD GOVERNOR DESIGN

#### A. Linearized Model

For the design of the load governor, the nonlinear model of the fuel cell (1) is linearized at a representative operating point. We choose nominal stack current as  $I_{fc}^o = 192$  A. The nominal value for oxygen excess ratio is selected at  $\lambda_{O_2}^o = 2.0$ , which provides

<sup>3</sup>The first strategy assumes that the future reference signal remains constant. Infeasibility of solution may arise because of the finite prediction horizon assumption. The second strategy does not make any assumption on future values of the reference. Moreover, if the initial conditions lie in the constraint admissible set, infeasibility would not arise, since by construction the admissible set is based on satisfying the constraints over a semi-infinite future horizon. A brief comparison of the two strategies can be found in [17].

maximum fuel cell net power for the nominal current [9]. The compressor motor voltage needed, to supply the optimum air flow that corresponds to  $I_{fc}^o$  and  $\lambda_{O_2}^o = 2.0$ , is  $v_{cm}^o = 164$  V. The linearized system has eight dynamic states<sup>4</sup> and is described by

$$\begin{aligned} \dot{x}_{ln} &= Fx_{ln} + G_u \delta v_{cm} + G_v \delta I_{fc} \\ y_{ln} &= Cx_{ln} + D_v \delta I_{fc} \end{aligned} \quad (2)$$

where

$$\begin{aligned} x_{ln} &= \delta [m_{O_2} \quad m_{H_2} \quad m_{N_2} \quad w_{cm} \quad p_{sm} \quad m_{sm} \quad m_{w,an} \quad p_{rm}]^T \\ y_{ln} &= \delta [W_{cp} \quad p_{sm} \quad \lambda_{O_2}] \end{aligned}$$

and  $\delta$  stands for the deviation from the operating point. The compressor control input  $v_{cm}$  is determined by a combination of feedforward and proportional plus integral (PI) feedback control action. The feedback controller is designed to ensure a closed-loop stable system. The discrete-time model of the closed-loop system is used for the design of the load governor

$$\begin{aligned} x(k+1) &= A_{cl}x(k) + B_v \delta I_{fc}(k) \\ y(k) &= Cx(k) + D_v \delta I_{fc}(k). \end{aligned} \quad (3)$$

### B. Constraints

Fig. 2 shows a compressor map with superimposed surge and choke constraint lines. In this map, each solid line curve represents a compressor rotational speed. The surge and choke boundaries are represented by dotted lines. We introduce constraints that confine operation of the compressor between the surge and choke lines and prevent stack starvation. The nonlinear surge boundary can be approximated by a straight line for the most part of the operating region as shown in Fig. 2. Both compressor flow and pressure ratio are functions of states of the system and are relatively easy to measure. The choke limit can be expressed similarly. The constraints can then be represented by two linear inequalities defined by the linear approximation

$$-0.0506\delta W_{cp} + \delta p_{sm} \leq 0.4, \quad 0.0155\delta W_{cp} - \delta p_{sm} \leq 0.73. \quad (4)$$

The lower limit of oxygen excess ratio is set to 1.9 to avoid large variations in the cathode oxygen partial pressure and, hence, stack oxygen starvation

$$\lambda_{O_2} \geq 1.9 \Rightarrow \delta \lambda_{O_2} \geq -0.1. \quad (5)$$

Equations (4) and (5) can be combined as follows:

$$\begin{bmatrix} -0.0506 & 1 & 0 \\ 0.0155 & -1 & 0 \\ 0 & 0 & -1 \end{bmatrix} y(k+j|k) \leq \begin{bmatrix} 0.4 \\ 0.73 \\ 0.1 \end{bmatrix}, \quad j=1, 2, \dots \quad (6)$$

where  $y(k+j|k)$  is the predicted value of the outputs at instant  $k+j$  based on information available at instant  $k$ .

<sup>4</sup>One of the states, the mass of water in the cathode, is unobservable during linearization and, therefore, does not appear in the linearized model.

### C. Linear Load Governor

Our goal is to determine the current  $I_{fc}$ , which is as close as possible to the current demand  $I_d$ , and does not violate the constraints. The reference modification can be accomplished via a first-order linear filter with a scalar adjustable bandwidth parameter  $\beta$

$$I_{fc}(k+1) = I_{fc}(k) + \beta(k)(I_d(k) - I_{fc}(k)) \quad (7)$$

and  $\beta(k) \in [0, 1]$ . Ideally,  $\beta(k) = 1$  meaning  $I_{fc}(k+1) = I_d(k)$  and the current command, only suffer a unit delay. When there is a large change in  $I_d$  and a possibility of future constraint violation exists,  $\beta$  is reduced to avoid constraint violation. In the extreme case when  $\beta(k) = 0$ , we have  $I_{fc}(k+1) = I_{fc}(k)$ . The parameter  $\beta(k)$  is maximized at each sample time  $k$ , subject to the condition that maintaining  $I_{fc}(j) = I_{fc}(k)$  for all  $j > k$  guarantees constraint satisfaction. The assumption at each instant is that measured current demand  $I_d(k)$ , stays constant over the future horizon.

The optimization can be solved in a few different ways. It can be arranged as a linear programming (LP) problem with the single variable  $\beta$  and the constraints (6) for a sufficiently large horizon, and solved online. Bisectional search for maximum constraint-admissible  $\beta$  is another possible online solution and is applicable to nonlinear systems as well [7]. Such online solutions may be computationally intensive for systems with more than a few states.

Fortunately, for linear systems, a large portion of calculations can be performed offline, thereby reducing the online computational effort. Specific procedures for such FRGs are detailed in [8] and are used here for the fuel cell application. We provide a brief summary of the methodology and refer the interested reader to [8] for details.

Future constraint violations can be predicted by checking if the state of the system belongs to a maximal output admissible set, called  $O_\infty$ . The  $O_\infty$  is the set of all initial states  $x(0)$ , and the modified reference  $\delta I_{fc}(0)$ , which with  $\beta = 0$  guarantees satisfaction of future constraints. It is defined as

$$O_\infty = \left\{ (x(0), \delta I_{fc}(0)) : y(k) = Cx(k) + D_v \delta I_{fc}(0) \in Y \forall k \in \mathbb{Z}^+ \right\} \quad (8)$$

where  $Y$  is the constraint set described by (6) and the state dynamics are those of (3). The set,  $O_\infty$ , is positively invariant for the system defined by (3) with  $\beta = 0$ . Thus, if the system starts in this set and the current  $I_{fc}$  is kept constant into the future, the trajectory will remain in  $O_\infty$  and the constraints will be satisfied.

The goal is to find the maximum value of  $\beta$  which maintains the state in  $O_\infty$

$$\beta^* = \max \left\{ \beta \in [0, 1] : \begin{bmatrix} A_{cl}x + B_v \delta I_{fc} \\ \delta I_{fc} \end{bmatrix} + \beta \begin{bmatrix} 0 \\ I_d - I_{fc} \end{bmatrix} \in O_\infty \right\}. \quad (9)$$

The set  $O_\infty$  does not, in general, admit a characterization by a finite set of linear inequalities (i.e., it may not be finitely determined). It does, however, have a computable approximation  $\check{O}_\infty$ , which is finitely determined, see [8].

The set  $\tilde{O}_\infty$  is derived from  $O_\infty$  using the following procedure. Let  $x_{ss}(\delta I_{fc}) = (I - A_{cl})^{-1} B_v \delta I_{fc}$  denote the steady-state value of the state for a constant  $\delta I_{fc}$  and let  $H_0 = C(I - A_{cl})^{-1} B_v + D_v$  be the dc gain of the plant from the input  $\delta I_{fc}$  to the output  $y$ . Then the set  $O_\infty$  admits the following characterization:

$$O_\infty = \left\{ (x, \delta I_{fc}) : H_0 \delta I_{fc} \in Y, H_0 \delta I_{fc} + CA_{cl}^t (x - x_{ss}(\delta I_{fc})) \in Y \quad \forall t \in \mathbb{Z}^+ \right\}.$$

Then,  $\tilde{O}_\infty$  is constructed as

$$\tilde{O}_\infty = \left\{ (x, \delta I_{fc}) : H_0 \delta I_{fc} \in (1 - \epsilon)Y, H_0 \delta I_{fc} + CA_{cl}^t (x - x_{ss}(\delta I_{fc})) \in Y \quad \forall t \in \mathbb{Z}^+ \right\}$$

where  $1 > \epsilon > 0$ . Under the assumptions that  $A_{cl}$  is asymptotically stable,  $Y$  is compact and  $0 \in \text{int}Y$  it can be shown that  $\tilde{O}_\infty \subset O_\infty$ , and that it is positively invariant and finitely determined. In other words,  $\tilde{O}_\infty$  can be represented by a finite number of linear inequalities and there exists a finite  $t^* \in \mathbb{Z}^+$  such that

$$\tilde{O}_\infty = \left\{ (x, \delta I_{fc}) : H_0 \delta I_{fc} \in (1 - \epsilon)Y, H_0 \delta I_{fc} + CA_{cl}^t (x - x_{ss}(\delta I_{fc})) \in Y, t = 0, 1, \dots, t^* \right\}.$$

The reason  $\tilde{O}_\infty$  is finitely determined is that due to the stability of  $A$ ,  $A^t \rightarrow 0$ , and, thus,  $H_0 \delta I_{fc} \in (1 - \epsilon)Y$  implies that the inequality constraint  $H_0 \delta I_{fc} + CA_{cl}^t (x - x_{ss}(\delta I_{fc})) \in Y$  becomes inactive for all  $t$  sufficiently large.

For a system with  $n$  states and linear constraints,  $\tilde{O}_\infty \subset \mathbb{R}^{n+1}$  is a polytope<sup>5</sup> with  $m$  faces represented as a set of solutions to a system of linear inequalities of the general form

$$\Phi_{m \times n+1} \begin{bmatrix} x(0) \\ \delta I_{fc}(0) \end{bmatrix} \leq \Theta_{m \times 1}. \quad (10)$$

For systems with large state dimension and high sampling rates, the number of inequalities in the representation of  $\tilde{O}_\infty$  can grow large. This is undesirable for two reasons: The effort to compute  $\beta(k)$  increases with the number of inequalities in the representation of  $\tilde{O}_\infty$  and ROM size to store a representation of  $\tilde{O}_\infty$  also increases with the number of inequalities in its representation. Often, however, some inequalities in the representation of  $\tilde{O}_\infty$  are almost redundant, i.e., if they are eliminated from the representation of  $\tilde{O}_\infty$  the resulting polytope is only slightly larger than  $\tilde{O}_\infty$ . Since the polytope resulting from such constraint elimination may not be a constraint-admissible set of initial conditions itself, it is scaled down uniformly in the  $x$ -direction (but not in the  $I_{fc}$  direction) until it is contained in  $\tilde{O}_\infty$ . After this process of inequality elimination and shrinkage, we obtain a polytope  $P$ , which is constraint admissible and has fewer inequalities compared to  $\tilde{O}_\infty$ . At the same time, one has to keep in mind that  $P$  is only a subset of  $\tilde{O}_\infty$  and, thus, can result in more conservative performance.

<sup>5</sup>A polytope may be defined as the convex hull of a finite set of points, or as a bounded intersection of a finite set of half-spaces.

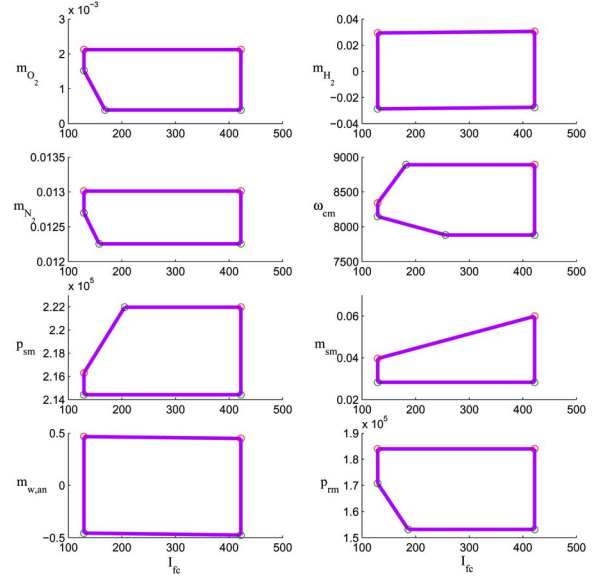


Fig. 6.  $\tilde{O}_\infty$  projected onto the state-current planes.

The set  $P$  may not be positively invariant. Thus, the situation may arise that a feasible  $\beta \in [0, 1]$  does not exist. In the event that the trajectory leaves the set  $P$ , in agreement with the theoretical results in [8], the RG sets  $\beta = 0$ .

Once  $\tilde{O}_\infty$  or  $P$  are determined, the online evaluation of  $\beta^*$  is relatively simple. A computationally efficient method for finding  $\beta^*$  is given in [8] which involves a fixed number of adds, subtracts, divides, multiples, max, and min operations in each sampling interval.

We next demonstrate the performance of the fast load governor in linear simulations. Once constraint satisfaction is shown in linear simulations, we explain the procedure for application of the linear load governor to the nonlinear plant.

## IV. LINEAR SIMULATION ANALYSIS

### A. Governor Performance

In this section, we analyze the performance of the fast load governor based on both the  $\tilde{O}_\infty$  and  $P$  admissible sets. The sampling frequency is fixed at 100 Hz. Constraints are surge, choke, and starvation constraints given in (6). The set  $\tilde{O}_\infty \subset \mathbb{R}^{11}$  is characterized by 348 linear inequalities ( $m = 348$ ) and is determined offline. Due to its large dimension, the admissible set  $\tilde{O}_\infty$  cannot be geometrically visualized. Instead, Fig. 6 shows its projection onto two dimensional state-current planes. In all graphs, the x-axis represents the current taken from the fuel cell and the y-axis shows the fuel cell states. We can see that the constraints of the system can be satisfied for a current up to 430 A. The limiting factor is the rate by which the current is increased. If the current is increased too quickly, the states leave the polygons shown and constraints may be violated.

Constraint elimination and a shrinkage factor of 1.2 generate  $P \subset \tilde{O}_\infty$  with only 77 linear inequalities. For comparison, shrinkage factors of 1.4, 1.75, 2.0, and 10 resulted in  $P$  with, respectively, 65, 51, 42, and 22 inequalities; the  $P$  corresponding to 1.2 was selected as the best compromise between the number of inequalities and conservatism of the RG operation.

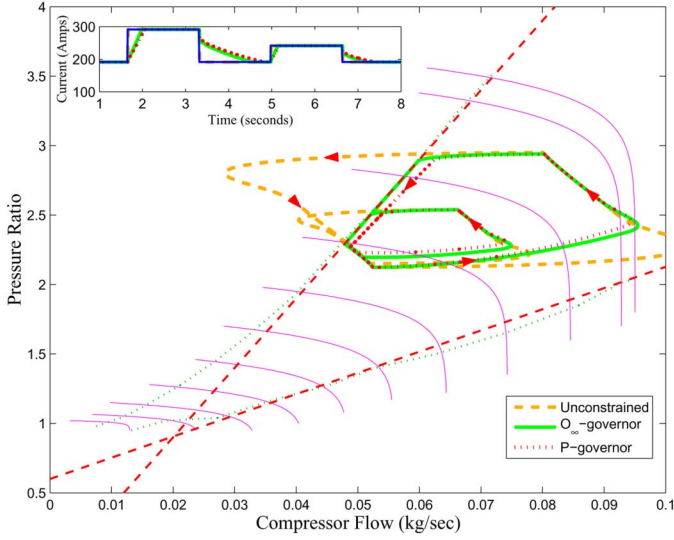


Fig. 7. Compressor pressure and flow trajectory for different load governor designs.

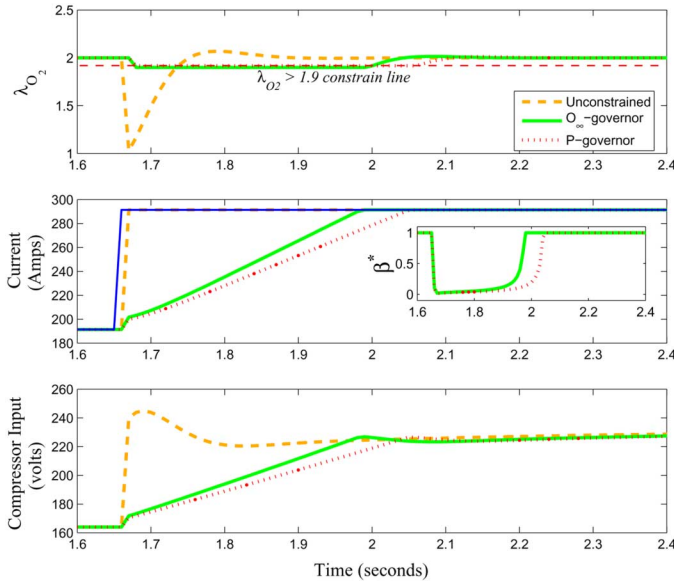


Fig. 8. Simulation during tip-in transient when oxygen starvation constraint is active.

We examine the performance of the fast load governor which uses  $\tilde{O}_\infty$  (subsequently referred to as  $\tilde{O}_\infty$ -governor), and fast load governor which uses  $P \subset \tilde{O}_\infty$  (subsequently referred to as  $P$ -governor) during a series of step-ups and step-downs in the current demand (which correspond to driver tip-in and tip-out commands, respectively) with maximum current step of 100 A.<sup>6</sup> Fig. 7 shows the compressor map during the entire load cycle. The current profile is shown at the top left corner.

Fig. 8 shows the oxygen excess ratio, current, and compressor motor command during the 100-A tip-in. The thin solid line is the actual current demand. The small insert plot shows the optimum values of the parameter  $\beta$ . In the plots, three different cases are shown: unconstrained, with  $\tilde{O}_\infty$ -governor, and with the  $P$ -governor. In the unconstrained case, the surge constraint

<sup>6</sup>A simple kinetic energy calculation shows that accelerating a 1000-kg vehicle from 20 to 21.5 m/s (45 to 48 mph) in 1 s, requires almost 100 A on a 300-V BUS that connects the fuel cell with a traction motor.

TABLE I  
NUMBER OF ONLINE FLOATING POINT OPERATIONS AND  
CPU TIME FOR DIFFERENT LOAD GOVERNOR DESIGNS

LG Design	Flops Avg.	per Max	sample time Min	Total CPU time (sec)
Fast LG with $\tilde{O}_\infty$ 348 inequalities 1 variable	8622	8808	8573	15.9
Fast LG with 1.2 Shrinkage 77 inequalities 1 variable	2082	2118	2069	4.0

is violated during tip-outs as is shown in the compressor map plot. Also, the oxygen starvation constraint is not met during the tip-in period and oxygen excess ratio almost reaches the critical value of 1. The  $\tilde{O}_\infty$ -governor and  $P$ -governor enforce all the constraints. The governor negotiates the constraints by moving along the constraint boundary. The  $P$ -governor performs more conservatively and avoids constraint violation by a certain margin. This happens because  $P \subset \tilde{O}_\infty$ . The advantage of the  $P$ -governor is in reduced online computation load as we will illustrate later.

### B. Computational Requirements

The computational requirements of each algorithm can be a deciding factor for which algorithm gets implemented. The computational load of an algorithm may be characterized by the number of floating point operations (flops) performed. In reference [8], the number of flops (multiplication, additions, comparisons) for online calculation of FRG is estimated to be  $(5n_v + 2n + 4) \times m$ , where  $n_v$ ,  $n$ , and  $m$  are the number of reference commands, total number of states, and total number of constraints. In the simulations presented so far,  $n_v = 1$  and  $n = 10$ . For the  $\tilde{O}_\infty$ -governor,  $m = 348$  and, therefore, the estimated number of flops is 10 092 per sampling instant. For the  $P$ -governor,  $m = 77$  and the number of flops reduces to 2233, an almost five-fold reduction. We also used the flops command in MATLAB<sup>7</sup> to get an estimate for the actual number of flops for different load governor designs.<sup>8</sup> The average, maximum, and minimum number of recorded flops is summarized in Table I. MATLAB also provides an estimate of the CPU time spent on running a selected portion of the code. The last column of Table I shows the total CPU time required for running a full simulation of the linear model and load governor on an 866-MHz Intel<sup>9</sup> Pentium III processor. It is shown that the CPU time spent on the calculations of the load governor are considerably reduced by moving from the  $\tilde{O}_\infty$ -governor to the  $P$ -governor.

The number of flops given by MATLAB has little variation from one step to another and appears to be relatively close to the theoretically estimated value. We note that 2082 flops at an update rate of 10 ms for the  $P$ -governor case is within the capability of automotive microcontrollers although this is still a rather large computational task. In fact, an optimized implementation in a production automotive micro-controller simulator showed that the  $\beta(k)$  can be calculated within 1.3 ms; and this calculation requires close to 4 kB of ROM (this represents

<sup>7</sup>MATLAB is a registered trademark of The MathWorks Inc., Natick, MA.

<sup>8</sup>The command flops is not supported in newer releases of MATLAB. We used the release 11.1 of MATLAB to get a flop count.

<sup>9</sup>Intel is a registered trademark of Intel Corporation, Santa Clara, CA.

the total size of the code size and constants). The computational effort involved can be further mitigated by changing the update rate. For example, it has been shown via simulations that the update rate of 20 ms still yields acceptable performance. Further, when  $\beta^* = 1$  and the reference is constant or varies slowly, then  $\beta^*$  can be kept equal to 1 without performing any calculation, thereby further reducing the computational load for the load governor case.

## V. APPLICATION OF THE FAST LOAD GOVERNOR TO THE NONLINEAR MODEL

The fast load governor design described previously, is based on the assumption that the plant is linear. In this section, we explain how the fast load governor can be modified and applied to the nonlinear model of the fuel cell system. Our focus will be on the  $\tilde{O}_\infty$ -governor, but the discussions apply to the  $P$ -governor as well.

Recall that in the  $\tilde{O}_\infty$ -based load governor, the parameter  $\beta^*$  was a function of the linear state of the system, current demand, current taken from the fuel cell, and  $\tilde{O}_\infty$ . In the first trial of the load governor on the nonlinear plant we used  $\tilde{O}_\infty$  to guard against constraint violation, while replacing the linear states with nonlinear states. While this approach worked well for small to medium deviations from the operating point (50-A steps in current demand up or down) it failed to perform satisfactorily for larger steps. Specifically, during a current step of 100 A,  $\beta^*$  was set to zero by the governor and the reference current tracking was lost. This was due to differences between linear and nonlinear systems which caused the nonlinear state to be outside of  $\tilde{O}_\infty$  in steady-state. Next, we attempted to remedy this situation by adjusting the nonlinear state by the difference between linear and nonlinear steady states. Using (3), the linear state equilibrium for a current level  $I_{fc}$  is  $x_{ss} = (I - A_{cl})^{-1} B_v \delta I_{fc}$ . The nonlinear equilibrium corresponding to  $I_{fc}$  was calculated offline by simulation under different loads and stored in a look-up table  $\Gamma(I_{fc})$ . In particular, we simulated the nonlinear plant model for 18 different values of  $\delta I_{fc}$  in the range of  $[-70, 100]$  and in increments of 10 A. After the plant reached steady-state for each value of current, we recorded the steady states in the look-up table. The adjusted state is then calculated according to

$$x_{adj}(k) = x_{nl}^{aug}(k) - \Gamma(I_{fc}(k)) + (I - A_{cl})^{-1} B_v \delta I_{fc}(k). \quad (11)$$

where  $x_{nl}^{aug}$  denotes the augmented states of the nonlinear fuel cell model and the compressor controller. Since  $\tilde{O}_\infty$  is constructed using the linear model, the nonlinear state  $x_{nl}^{aug}$  is adjusted by subtracting the nonlinear steady-state  $\Gamma(I_{fc}(k))$ , and adding the linear steady-state  $(I - A_{cl})^{-1} B_v \delta I_{fc}(k)$ , then this adjusted state along with  $\tilde{O}_\infty$  is used to find the value of  $\beta$ .<sup>10</sup>

Note that even with the adjustment given by (11), the dynamics of the process are still predicted by the linearized model. Figs. 9 and 10 show the compressor trajectory and the time response of the nonlinear plant for a series of step-ups and downs in demand. Figs. 9 and 10 show that the load governor modified by (11) is able to reduce large excursion into the surge region during the step of 100 A and that it reduces (but fails to eliminate) oxygen starvation constraint violation of 1.9 during

<sup>10</sup>In other words, we are shifting the polytope  $\tilde{O}_\infty$  in the state-space by the difference  $\Gamma(I_{fc}(k)) - (I - A_{cl})^{-1} B_v \delta I_{fc}(k)$ .

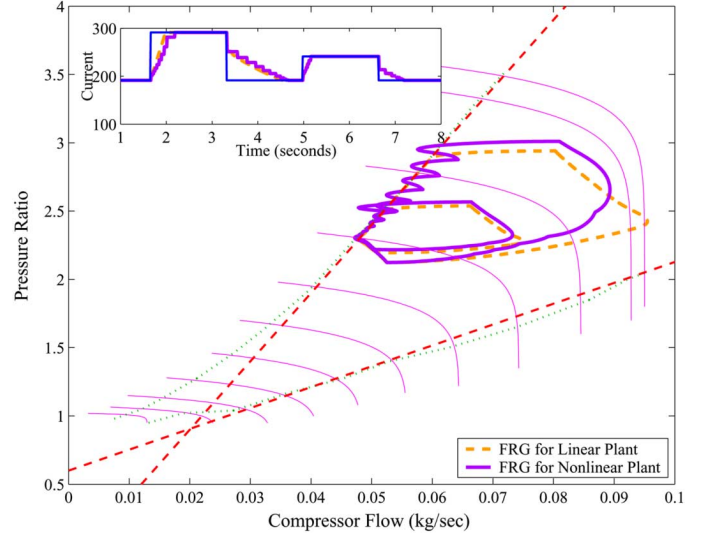


Fig. 9. Compressor pressure and flow trajectory with the load governor adjusted through (11).

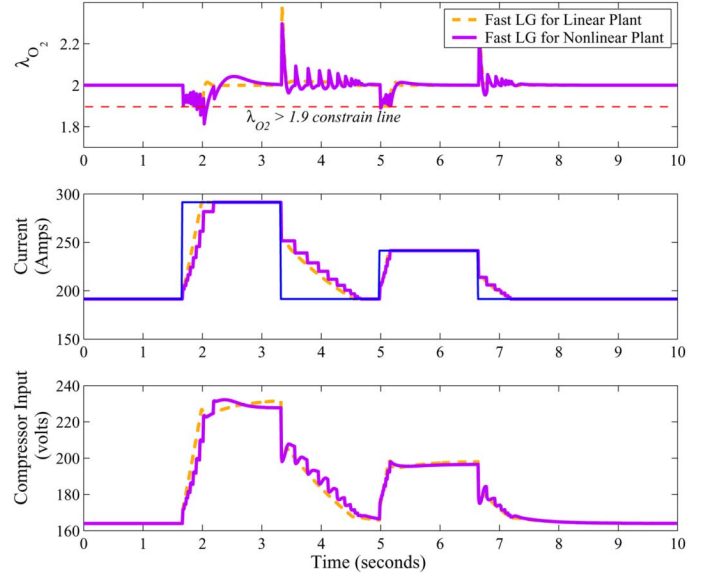


Fig. 10. Simulations for the case of the load governor adjusted by (11).

the first most aggressive tip-in. The load governor enforces the oxygen starvation constraint during other, less aggressive tip-ins. The system response, however, is jittery, since the load governor often and sporadically sets  $\beta$  to zero. Moreover, it is not realistic to assume all the states of the nonlinear plant can be measured.

Finally, to improve our results, another approach was pursued wherein the difference between the nonlinear plant and its linear model was reflected in the construction of  $\tilde{O}_\infty$ . Specifically, we redefined  $O_\infty$  as follows:

$$O_\infty = \left\{ (x, \delta I_{fc}, d) : y(k) = Cx(k) + D_v \delta I_{fc} + d \in Y \quad \forall k \in \mathbb{Z}^+ \right\} \quad (12)$$

where  $d$  is a constant output disturbance term. At each instant  $k$  during online calculations, the disturbance  $d$  is the difference between the plant output and the output predicted by the linear model

$$d(k) = y_{nl}(k) - (y_{ln}(k) + y^o). \quad (13)$$

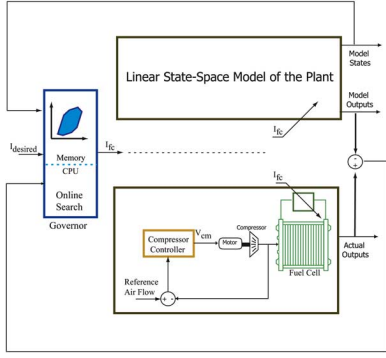


Fig. 11. Schematics of the plant, linear model, and the RG and their interactions.

where  $y^o$  denotes the value of the outputs at the operating point. The dimension of the admissible set is increased by the number of outputs  $n_y$ , i.e.,  $\tilde{O}_\infty \subset \mathbb{R}^{n+1+n_y}$ . The governor parameter  $\beta$  is determined as follows:

$$\beta^* = \max \left\{ \beta \in [0, 1] : \begin{bmatrix} A_{cl}x + B_v \delta I_{fc} \\ \delta I_{fc} \\ d \end{bmatrix} + \beta \begin{bmatrix} 0 \\ I_d - I_{fc} \\ 0 \end{bmatrix} \in \tilde{O}_\infty \right\} \quad (14)$$

where in (14) we use the state predicted by the linear model and account for the mismatch between the plant and the model via the disturbance term  $d$ . This approach is intended to reduce the governor sensitivity to model uncertainty which in our case is the mismatch between the linear and nonlinear models. This correction can help in eliminating constraint violation and jitter in the response.

Fig. 11 shows the schematic of this implementation. The load governor stores the system matrices that represent the linearized model of the plant in addition to the inequalities describing the set  $\tilde{O}_\infty$  (or  $P$ ). The maximum value of  $\beta \in [0, 1]$  is calculated based on the current demand  $I_d$ , linear model states  $x_{ln}$ , and the difference between the plant and model outputs  $d$ . Consequently, the allowable fuel cell current  $I_{fc}$  is determined and applied to both the nonlinear plant and the linearized model. The process is repeated at each sampling time.<sup>11</sup>

Figs. 12 and 13 show the simulation results and confirm that surge constraint violation is considerably reduced and that oxygen starvation constraint violation and jitter are eliminated. Note also that for this implementation of the governor, only the state predicted by the linear model and the measurement of the output  $y_{nl}(k)$  are needed; the full plant state (i.e., state of the nonlinear model) does not need to be known.

Note that by including the  $d$ -term the number of online computations increases by approximately  $2n_d \times m$ , where  $n_d$  is the dimension of the disturbance vector (number of measured outputs) and  $m$  is the total number of constraints. The approximate number of flops is then  $(5n_v + 2n_d + 2n + 4) \times m$ .

## VI. REDUCED-ORDER LOAD GOVERNOR

One possible way of reducing the number of computations is to use a low-order linear fuel cell model for construction of the load governor.

<sup>11</sup>Note that adding an output injection term to the linear model is another possibility which may further reduce the estimation error.

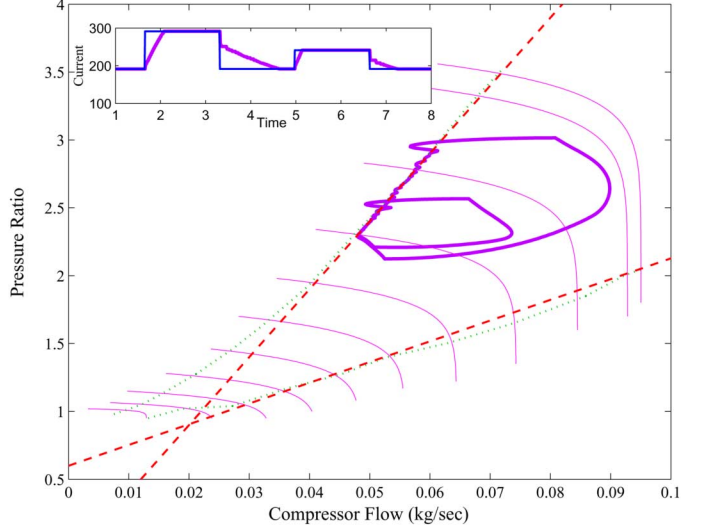


Fig. 12. Compressor flow trajectory when the generalized load governor is used. The surge excursion is noticeably reduced when the disturbance observer is used.

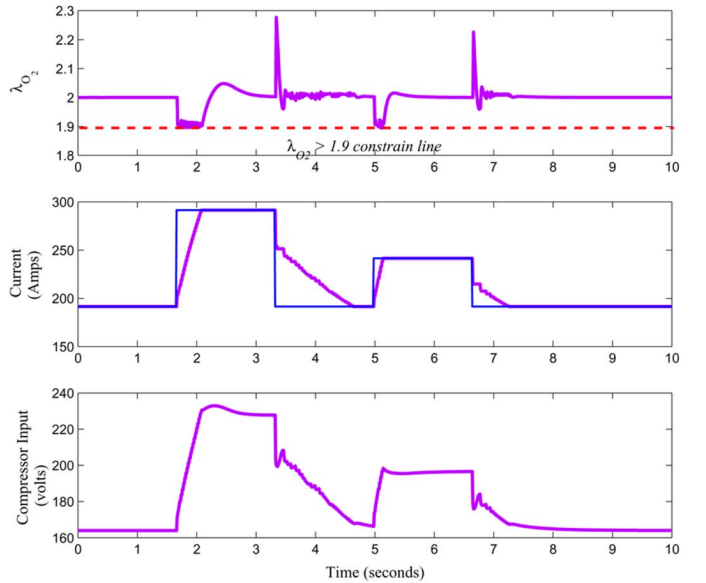


Fig. 13. Performance of the generalized fast load governor in nonlinear simulations without state-feedback. Inclusion of the disturbance term eliminates constraint violation.

The nine-state fuel cell model discussed so far, represents the anode, cathode, and return manifold dynamics in addition to the compressor and inlet manifold dynamics. While these subsystems interact, the compressor and oxygen flow dynamics might still be approximated well by a lower-order model. A reduced model of the nine-state fuel cell system is obtained in [18] for simulation of the air supply side. The reduced model has only four dynamic states: partial oxygen pressure inside the cathode  $p_{O_2}$ , partial nitrogen pressure inside the cathode  $p_{N_2}$ , compressor motor speed  $\omega_{cp}$ , and the supply manifold pressure  $p_{sm}$ . Fig. 14 compares the response of this reduced four-state model to the original nine-state model. Only during the two intervals of step-down in current (between the third and fourth seconds and sixth and seventh seconds), the response of the two

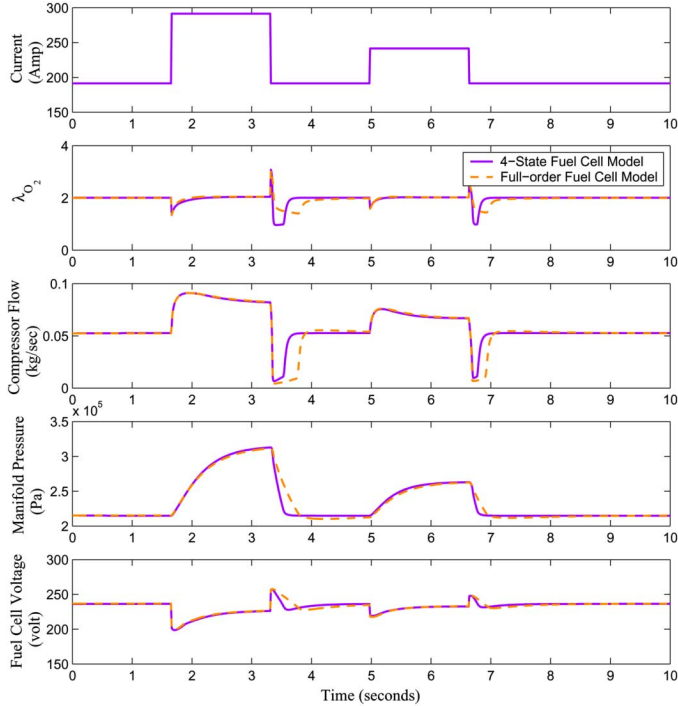


Fig. 14. Comparison of the original model and the four-state reduced model.

models is different. The reason for this difference may be attributed to the fact that during these two intervals, the compressor enters the surge region where the models are highly nonlinear. Therefore, a small mismatch in the supply manifold pressure can cause large deviations in the compressor flow and the oxygen excess ratio response. The interesting question that arises here is, if an RG designed based on the reduced model can enforce constraints of the full-order fuel cell system. If this is in fact possible, we may reduce the computations further by using a reduced-order load governor.

To address this question, we designed new  $\tilde{O}_\infty$  and  $P$ -governors based on a linearized approximation of the reduced-model. We then applied the reduced-order governors for constraint enforcement of the full-order nonlinear model. The difference between the two models was compensated by the disturbance term described by (13).

Figs. 15 and 16 show the performance of the reduced  $\tilde{O}_\infty$  and  $P$  governors when applied to the full-order nonlinear fuel cell model. The reduced-order  $\tilde{O}_\infty$ -governor satisfies the constraints of the full-order nonlinear model except during rapid step-downs in current when the surge constraint is instantaneously violated.<sup>12</sup> The  $\tilde{O}_\infty$ -governor allows operation of the compressor near the surge line, the drawback is that a small disturbance can result in the compressor surge. The  $P$ -governor, on the other hand, is more conservative. As a result, it was able to satisfy the constraints (practically at all times) during large disturbances even though it was designed for a reduced-order model of the plant.

When using the reduced model, the closed-loop system has a total of 5 states (4 model states and 1 compressor controller

<sup>12</sup>The excursion into the surge region lasts not more than a few sampling times in our simulations. In practice, once the compressor starts to surge, the recovery may take much longer.

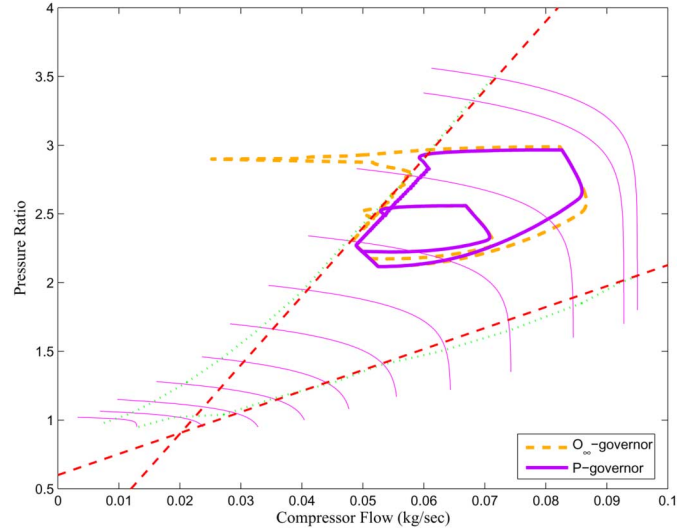


Fig. 15. Compressor pressure and flow trajectory when reduced governors are applied to the full-order nonlinear model.

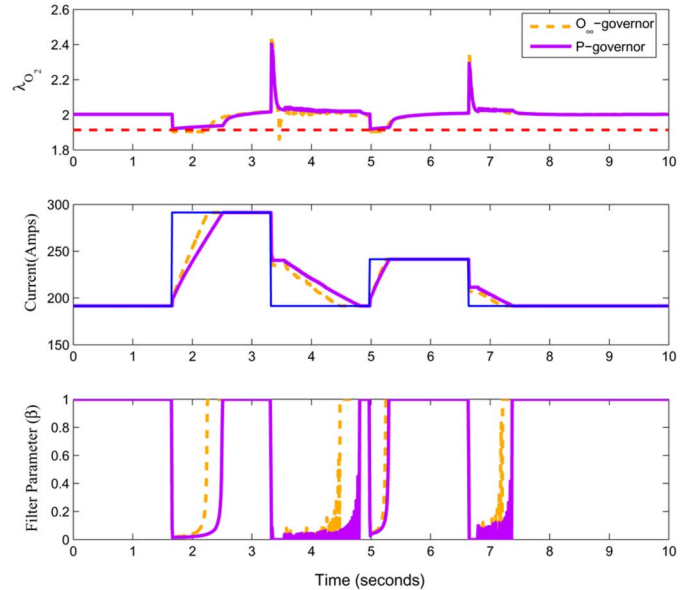


Fig. 16. Time history of response when reduced governors are applied to the full-order nonlinear model.

TABLE II  
COMPUTATIONS FOR FULL- AND REDUCED-ORDER GOVERNORS

LG	Model	d-term	$n_v$	$n_d$	$n$	$m$	Flops
$\tilde{O}_\infty$	Full	No	1	0	10	348	10092
$\tilde{O}_\infty$	Full	Yes	1	3	10	399	13965
$\tilde{O}_\infty$	Reduced	Yes	1	3	5	404	10100
$P$	Full	No	1	0	10	77	2233
$P$	Reduced	Yes	1	3	5	66	1650

state). Therefore, the  $\tilde{O}_\infty$  set which includes the disturbance term belongs to  $\mathbb{R}^9$  and is characterized by 404 linear constraints. Constraint elimination and shrinkage factor of 1.2 resulted in the approximation of  $P \subset \tilde{O}_\infty$  with only 66 constraints. Table II compares the number of flops (per sampling time) calculated analytically for the full- and reduced-order governors and shows that the required number of online computations for the reduced governors is considerably lower. In

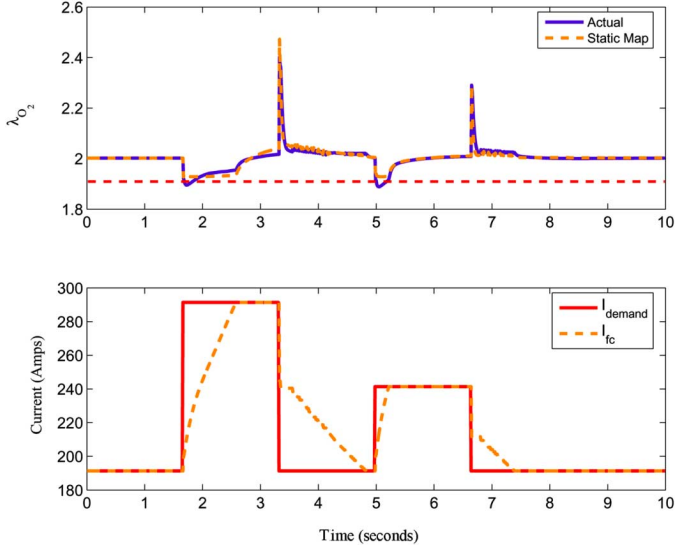


Fig. 17. Response when oxygen excess ratio is not measured and is estimated using a static map.

the case of the limited computational resource (which is usually the case in real-time implementation), the governor with the least computational effort is recommended.

## VII. OBSERVER DESIGN

The FRG described above requires measurements of all the constrained outputs. While the compressor flow and manifold pressure are relatively easy to measure, oxygen excess ratio is not a measured variable. Simulations show that there is a correlation between stack voltage and oxygen excess ratio. Hence, we used stack voltage, compressor flow, and manifold pressure to construct an observer for oxygen excess ratio. We first tried a Kalman filter based on the linearized reduced-order fuel cell model. During sudden transients the Kalman filter over estimated the drop in oxygen excess ratio, leading to conservative RG action. In our next attempt, we used the measurements from the full-order fuel cell model and a least square curve fit to construct a static map which relates oxygen excess ratio to compressor air flow (kilograms per second), manifold pressure (bar), stack voltage (volt), and stack current (amp) as follows:

$$\hat{\delta}\lambda_{O_2} = 18.061\delta W_{cp} + 0.592\delta p_{sm} - 0.0045\delta V_{st} - 0.0108\delta I_{fc}.$$

The static map could predict oxygen excess ratio in different test cycles closely; based on its performance and simplicity, we chose the linear static map over the more complicated observer designs. Fig. 17 shows the response of the reduced  $P$ -governor (applied to the full-order fuel cell model) when the static map was used to estimate oxygen excess ratio. The oxygen excess ratio is estimated with small error, as a result, the FRG is able to enforce the lower bound on oxygen excess ratio.

## VIII. REAL-TIME SIMULATIONS

Our analysis of the computational effort has so far been based on an approximate flop count. While this approach provides

TABLE III  
MODEL VARIABLES AND PARAMETERS

$A_{fc}$	active area of the fuel cell
$C_D$	nozzle discharge coefficient
$D_w$	diffusion coefficient
$F$	Farady number
$I$	current
$J$	compressor inertia
$M$	molar mass
$P$	power
$R$	universal gas constant
$T$	temperature
$V$	volume
$W$	mass flow rate
$d_c$	compressor diameter
$i$	fuel cell current density ( $I/A_{fc}$ )
$m$	mass
$n$	number of cells
$n_d$	electro-osmotic coefficient
$p$	pressure
$t_m$	membrane thickness
$v$	voltage
$\Omega$	humidity ratio
$\gamma$	ratio of gas heat capacity
$\phi$	relative humidity
$\omega$	rotational speed
$\rho_a$	air density
Sub/Super scripts	
$H_2$	Hydrogen
$N_2$	Nitrogen
$O_2$	Oxygen
$v$	vapor
$w$	water
$in$	incoming
$out$	outgoing
$rct$	reacted
$mbr$	exchanged through membrane
$purge$	purged
$an$	anode
$ca$	cathode
$cm$	compressor motor
$cp$	compressor
$fc$	fuel cell
$rm$	return manifold
$sm$	supply manifold
$st$	stack

useful insights into computational efficiency of different algorithms, it does not provide conclusive results on the CPU usage on a real-time platform. To obtain a more realistic estimate of computational requirements of the FRG, we also carried out the simulations on a real-time Opal-RT platform. The target processor was a 2.1-GHz processor running QNX real-time operating system. The simulations were executed at a fixed integration step of 0.01 s. The processor was able to calculate the modified reference  $v$ , in a fraction of a sampling time. For the  $P$ -governor implementation, for example, the combined simulation time for the plant and the governor was around 130 ms. Of this total time, only 14% were spent on running the linear model and the governor, while the rest was used to run the plant model. In other words, the effective computational time for the governor was almost 1/500 of the sampling interval on the real-time 2.1-GHz processor.

TABLE IV  
CALCULATION OF COMPRESSOR FLOW

Description	Equation	Eq. No.
Temperature Correction Factor	$\theta = T_{cp,in}/(288K)$	(A-6)
Pressure Correction Factor	$\delta = p_{cp,in}/(1atm)$	(A-7)
Compressor Speed Correction(rpm)	$N_{cr} = N_{cp}/\sqrt{\theta}$	(A-8)
Air Mass Flow	$W_{cp} = W_{cr}\delta/\sqrt{\theta}$	(A-9)
Corrected Air mass flow	$W_{cr} = \Phi\rho_a\frac{\pi}{4}d_c^2U_c$	(A-10)
Compressor Blade Speed (m/s)	$U_c = \frac{\pi}{60}d_cN_{cr}$	(A-11)
Normalized flow rate	$\Phi = \Phi_{max} \left[ 1 - \exp\left(\beta\left(\frac{\Psi}{\Psi_{max}} - 1\right)\right) \right]$	(A-12)
Dimensionless head parameter	$\Psi = \frac{C_p T_{cp,in} \left[ \left(\frac{p_{cp,out}}{p_{cp,in}}\right)^{\frac{\gamma-1}{\gamma}} - 1 \right]}{\frac{1}{2}U_c^2}$	(A-13)
Polynomial functions	$\Phi_{max} = a_4M^4 + a_3M^3 + a_2M^2 + a_1M + a_0$	(A-14)
	$\beta = b_2M^2 + b_1M + b_0$	(A-15)
	$\Psi_{max} = c_5M^5 + c_4M^4 + c_3M^3 + c_2M^2 + c_1M + c_0$	(A-16)
Inlet Mach Number	$M = \frac{U_c}{\sqrt{\gamma R_a T_{cp,in}}}$	(A-17)

## IX. CONCLUSIONS

This paper presented the design of a load governor for preventing oxygen starvation and compressor surge and choke in fuel cell systems. The main design objective was to enforce these constraints without compromising performance when constraints are inactive and with minimal computational burden on a microcontroller. To meet these requirements the maximal constraint admissible set design procedure was used. For linear systems this approach allows carrying a large portion of computations offline, thus, reducing the online computation burden. We first employed the idea of such fast load governors on a linearized fuel cell model and provided some insight into computational requirements. When applied to the nonlinear plant model, the load governor required an adjustment to compensate for differences between the linear model and the nonlinear system. Introducing a step disturbance observer in the load governor design allowed to nearly eliminate constraint violation and jitter in the response. The step disturbance observer eliminated the need for measurement or estimation of the plant states as well. We then showed that the computations could be further reduced by using a lower-order model in designing the load governor. Overall, we showed that the number of computational flops could be reduced 6–8 times without much sacrifice on the performance by moving to a reduced load governor. It was shown that with the proposed design the load governor computations can be easily handled in real-time on a rapid prototyping platform. Feasibility of computations on an automotive microcontroller was also established by running the governor in a production microcontroller simulator. While the results were specific to the fuel cell problem, the insights into the computational requirements and the design procedure for fast load governors applied to nonlinear plants may also be useful in other applications.

## APPENDIX

This appendix provides a summary of the compressor and the fuel cell models governing equations and parameters. The models and parameters are explained in more detail in [9]. Table III lists the parameters and variables of the model.

*The Compressor Model:* The compressor air flow  $W_{cp}$  and its temperature  $T_{cp}$  are determined using a nonlinear model for

the compressor which has been developed in [9] for an allied signals centrifugal compressor that has been used in a fuel cell vehicle [19].

The compressor outlet temperature and the torque required to drive the compressor are calculated using standard thermodynamic equations [20], [21]. The temperature of the air leaving the compressor is calculated as follows:

$$T_{cp} = T_{atm} + \frac{T_{atm}}{\eta_{cp}} \left[ \left( \frac{p_{sm}}{p_{atm}} \right)^{(\gamma-1/\gamma)} - 1 \right] \quad (A-1)$$

where  $p_{atm}$  is the inlet atmospheric pressure,  $p_{sm}$  is the outlet pressures,  $\gamma = 1.4$  is the ratio of the specific heats of air,  $\eta_{cp}$  is the compressor efficiency, and  $T_{atm}$  is the atmospheric temperature. The compressor driving torque  $\tau_{cp}$  is

$$\tau_{cp} = \frac{C_p}{\omega_{cp}} \frac{T_{atm}}{\eta_{cp}} \left[ \left( \frac{p_{sm}}{p_{atm}} \right)^{(\gamma-1/\gamma)} - 1 \right] W_{cp} \quad (A-2)$$

where  $\omega_{cp}$  is the compressor rotational speed,  $W_{cp}$  is the compressor flow, and  $C_p$  is the specific heat capacity of air. The compressor rotational speed  $\omega_{cp}$  is determined as a function of compressor motor torque  $\tau_{cm}$  and the torque required to drive the compressor  $\tau_{cp}$

$$J_{cp} \frac{d\omega_{cp}}{dt} = \tau_{cm} - \tau_{cp} \quad (A-3)$$

where  $J_{cp}$  is the compressor inertia. The compressor motor torque  $\tau_{cm}$  is calculated as a function of motor voltage  $v_{cm}$  using a dc motor model

$$\tau_{cm} = \eta_{cm} \frac{k_t}{R_{cm}} (v_{cm} - k_v \omega_{cm}) \quad (A-4)$$

where  $k_t$ ,  $R_{cm}$ , and  $k_v$  are the motor constants and  $\eta_{cm}$  is the motor mechanical efficiency.

The compressor air mass flow rate  $W_{cp}$  is determined as a function of pressure ratio across the compressor and blade speed, using a compressor map shown in Fig. 2. In this map, the dashed lines represent boundaries beyond which compressor surge and choke can occur. The equations used here to represent compressor dynamics are valid within these bounds. Enforcement of point-wise-in-time constraints as explained in the paper ensured operation of the compressor inside the bounded region

TABLE V  
FUEL CELL MODEL GOVERNING EQUATIONS

Physical Law Applied to	Equation	Eq. No
Conservation of Mass: Cathode/Oxygen	$\frac{dm_{O_2}}{dt} = W_{O_2,in} - W_{O_2,out} - W_{O_2,rct}$	(A-18)
Conservation of Mass: Cathode/Nitrogen	$\frac{dm_{N_2}}{dt} = W_{N_2,in} - W_{N_2,out}$	(A-19)
Conservation of Mass: Cathode/Vapor	$\frac{dm_{w,ca}}{dt} = W_{v,ca,in} - W_{v,ca,out} + W_{v,gen} + W_{v,mbr}$	(A-20)
Conservation of Mass: Supply Manifold	$\frac{dm_{sm}}{dt} = W_{cp} - W_{sm}$	(A-21)
Conservation of Energy: Manifold Pressure	$\frac{dp_{sm}}{dt} = \gamma R (W_{cp} T_{cp} - W_{sm} T_{sm}) / (M_a^{atm} V_{sm})$	(A-22)
Conservation of Energy: Air Compressor	$J_{cp} \frac{d\omega_{cp}}{dt} = \frac{1}{\omega_{cp}} (P_{cm} - P_{cp})$	(A-23)
Conservation of Energy (Isothermal): Return Manifold Pressure	$\frac{dp_{rm}}{dt} = RT_{st} (W_{ca} - W_{rm}) / (M_a^{ca} V_{rm})$	(A-24)
Conservation of Mass: Hydrogen in the Anode	$\frac{dm_{H_2}}{dt} = W_{H_2,in} - W_{H_2,purge} - W_{H_2,rct}$	(A-25)
Conservation of Mass: Vapor in the Anode	$\frac{dm_{w,an}}{dt} = W_{v,an,in} - W_{v,purge} - W_{v,mbr}$	(A-26)
Psychrometric Law: Vapor Pressure	$p_{v,ca} = \min [1, m_{w,ca} RT_{st} / (M_v V_{ca} p_{sat}^{st})] p_{sat}^{st}$	(A-27)
Dalton Law: Cathode Pressure	$p_{ca} = p_{O_2} + p_{N_2} + p_{v,ca}$	(A-28)
Ideal Gas Law: Oxygen Pressure	$p_{O_2} = \frac{RT_{st}}{M_{O_2} V_{ca}} m_{O_2}$	(A-29)
Ideal Gas Law: Nitrogen Pressures	$p_{N_2} = \frac{RT_{st}}{M_{N_2} V_{ca}} m_{N_2}$	(A-30)
Ideal Gas Law: Manifold Air Temperature	$T_{sm} = \frac{p_{sm} V_{sm} M_a^{atm}}{R m_{sm}}$	(A-31)
Dalton/Ideal Gas Laws: Anode	$p_{an} = \frac{RT_{st}}{M_{H_2} V_{an}} m_{H_2} + \min \left[ 1, \frac{RT_{st} m_{w,an}}{M_v V_{an} p_{sat}^{st}} \right] p_{sat}^{st}$	(A-32)
Sub-Critical Nozzle Eq.(linearized) Supply Manifold Outlet	$W_{sm} = k_{sm} (p_{sm} - p_{ca})$	(A-33)
Sub-Critical Nozzle Eq.: Return Manifold Flow	$W_{rm} = \frac{C_{D,rm} A_{T,rm} P_{rm}}{\sqrt{RT_{rm}}} \left( \frac{p_{atm}}{P_{rm}} \right)^{\frac{1}{\gamma}} \left\{ \frac{2\gamma}{\gamma-1} \left[ 1 - \left( \frac{p_{atm}}{P_{rm}} \right)^{\frac{\gamma-1}{\gamma}} \right] \right\}^{\frac{1}{2}}$	(A-34)
Critical Nozzle Eq.	$W_{rm} = \frac{C_{D,rm} A_{T,rm} P_{rm}}{\sqrt{RT_{rm}}} \gamma^{\frac{1}{2}} \left( \frac{2}{\gamma+1} \right)^{\frac{\gamma+1}{2(\gamma-1)}}$	(A-35)
Partial Oxygen Flow	$W_{O_2,in} = 0.21 \frac{M_{O_2}}{0.21 M_{O_2} + 0.79 M_{N_2}} \frac{1}{1 + \Omega_{atm}} W_{sm}$	(A-36)
Partial Nitrogen Flow	$W_{N_2,in} = 0.79 \frac{M_{N_2}}{0.21 M_{O_2} + 0.79 M_{N_2}} \frac{1}{1 + \Omega_{atm}} W_{sm}$	(A-37)
Partial Vapor Flow	$W_{v,ca,in} = \frac{\Omega_{ca,in} W_{sm}}{1 + \Omega_{atm}}$	(A-38)
Atmospheric Humidity Ratio	$\Omega_{atm} = \frac{M_v}{M_a} \frac{\phi_{atm} p_{sat}^{atm} / p_{atm}}{1 - \phi_{atm} p_{sat}^{atm} / p_{atm}}$	(A-39)
Cathode Humidity Ratio	$\Omega_{ca,in} = \frac{M_v}{M_a} \frac{\phi_{ca,in} p_{sat}^{st}}{p_{sm} (1 - \phi_{atm} p_{sat}^{st} / p_{atm})}$	(A-40)
Oxygen Outflow	$W_{O_2,out} = \frac{m_{ca}}{m_{ca}} W_{ca}$	(A-41)
Nitrogen Outflow	$W_{N_2,out} = \frac{m_{ca}}{m_{ca}} W_{ca}$	(A-42)
Vapor Outflow	$W_{v,ca,out} = \frac{p_{v,ca} V_{ca} M_v}{RT_{st} m_{ca}} W_{ca}$	(A-43)
Reacted Oxygen	$W_{O_2,rct} = M_{O_2} \frac{n_{Ist}}{4F}$	(A-44)
Reacted Hydrogen	$W_{H_2,rct} = M_{H_2} \frac{n_{Ist}}{2F}$	(A-45)
Vapor Generated	$W_{v,gen} = M_v \frac{n_{Ist}}{2F}$	(A-46)
Mass Transport: Vapor diffusion	$W_{v,membr} = M_v A_{fc} n \left( n_d \frac{i}{F} - D_w \frac{\phi_{ca} - \phi_{an}}{t_m} \right)$	(A-47)
Hydrogen flow	$W_{H_2,in} = \frac{1}{1 + \Omega_{an,in}} W_{an,in}$	(A-48)
Anode Vapor flow	$W_{v,an,in} = \frac{\Omega_{an,in}}{1 + \Omega_{an,in}} W_{an,in}$	(A-49)
Anode Humidity Ratio	$\Omega_{an,in} = \frac{M_v}{M_{H_2}} \frac{\phi_{an,in} p_{sat}^{an,in}}{p_{an,in}}$	(A-50)
Dead-ended anode	$W_{v,purge} = 0$	(A-51)

and away from the surge and choke regions. In our simulations, this map is modeled using a nonlinear curve-fitting technique, which calculates compressor air flow as a function of inlet pressure  $p_{atm}$ , outlet pressures  $p_{sm}$ , and compressor rotational speed  $\omega_{cp}$

$$W_{cp} = f \left( \frac{p_{sm}}{p_{atm}}, \omega_{cp} \right). \quad (A-5)$$

The details of compressor flow calculation are shown in Table IV. A summary of fuel cell governing equations is provided in Table V.

#### ACKNOWLEDGMENT

The authors would like to thank Prof. J. Sun of the University of Michigan for his useful suggestions and for giving us access to the Opal-RT platform. They would also like to acknowledge C. Cox of Ford Motor Company who performed the assessment

of the load governor C-code implementation in the production microcontroller simulator.

#### REFERENCES

- [1] G. Boehm, D. Wilkinson, S. Khight, R. Schamm, and N. Fletcher, "Method and apparatus for operating a fuel cell," U.S. 6,461,751, Oct. 8, 2002.
- [2] J. Pukrushpan, A. Stefanopoulou, and H. Peng, "Control of fuel cell breathing," *IEEE Contr. Syst. Mag.*, vol. 24, no. 2, pp. 30–46, Apr. 2004.
- [3] A. Vahidi, A. Stefanopoulou, and H. Peng, "Model predictive control for starvation prevention in a hybrid fuel cell system," in *Proc. Amer. Contr. Conf.*, 2004, pp. 834–839.
- [4] P. Moraal and I. Kolmanovsky, Turbocharger modeling for automotive control applications, SAE, International, Warrendale, PA, Tech. Rep. 1999-01-0908, 1999.
- [5] B. de Jager, "Rotating stall and surge control: A survey," in *Proc. 34th Conf. Dec. Contr.*, 1995, pp. 1857–1862.
- [6] J. T. Gravdahl and O. Egeland, "Centrifugal compressor surge and speed control," *IEEE Trans. Contr. Syst. Technol.*, vol. 7, no. 5, pp. 567–579, Sep. 1999.

- [7] J. Sun and I. Kolmanovsky, "A robust load governor for fuel cell oxygen starvation protection," in *Proc. Amer. Contr. Conf.*, 2004, pp. 828–833.
- [8] E. Gilbert and I. Kolmanovsky, "Fast reference governors for systems with state and control constraints and disturbance inputs," *Int. J. Robust Nonlinear Contr.*, vol. 9, pp. 1117–1141, 1999.
- [9] J. Pukrushpan, A. Stefanopoulou, and H. Peng, *Control of Fuel Cell Power Systems: Principles, Modeling, Analysis, and Feedback Design*. London, U.K.: Springer-Verlag, 2004.
- [10] J. Pukrushpan, H. Peng, and A. Stefanopoulou, "Control-oriented modeling and analysis for automotive fuel cell systems," *ASME J. Dyn. Syst., Meas., Contr.*, vol. 126, pp. 14–25, 2004.
- [11] A. Bemporad, A. Casavola, and E. Mosca, "A predictive reference governor for constrained control systems," *Comput. Ind.*, vol. 36, pp. 55–64, 1998.
- [12] A. Bemporad, "Reference governor for constrained nonlinear systems," *IEEE Trans. Autom. Contr.*, vol. 43, no. 3, pp. 415–419, Mar. 1998.
- [13] A. Casavola and E. Mosca, "Reference governor for constrained uncertain linear systems subject to bounded input disturbances," in *Proc. 35th Conf. Dec. Contr.*, 1996, pp. 3531–3536.
- [14] E. Gilbert and K. Tan, "Linear systems with state and control constraints: the theory and applications of maximal output admissible sets," *IEEE Trans. Autom. Contr.*, vol. 36, no. 9, pp. 1008–1020, Sep. 1991.
- [15] E. Gilbert and I. Kolmanovsky, "Nonlinear tracking control in the presence of state and control constraints: A generalized reference governor," *Automatica*, vol. 38, pp. 2063–2073, 2002.
- [16] I. Kolmanovsky and E. Gilbert, "Theory and computation of disturbance invariant sets for discrete-time linear systems," *Math. Problems Eng.*, vol. 4, pp. 317–367, 1998.
- [17] J. Rossiter and B. Kouvaritakis, "Reference governors and predictive control," in *Proc. Amer. Contr. Conf.*, 1998, pp. 3692–3693.
- [18] K.-W. Suh and A. Stefanopoulou, "Coordination of converter and fuel cell controllers," *Int. J. Energy Res.*, vol. 29, pp. 1167–1189, 2005.
- [19] J. Cunningham, M. Hoffman, R. Moore, and D. J. Friedman, Requirements for flexible and realistic air supply model for incorporation into a fuel cell vehicle (FCV) system simulation, SAE, International, Warrendale, PA, Tech. Rep. 1999-01-2912, 1999.
- [20] M. Boyce, *Gas Turbine Engineering Handbook*. Houston, TX: Gulf, 1982.
- [21] J. Gravdahl and O. Egeiland, *Compressor Surge and Rotating Stall*. London, U.K.: Springer-Verlag, 1999.



and energy systems.

**Ardalan Vahidi** received the B.S. and M.S. degrees in civil engineering from Sharif University, Tehran, Iran, in 1996 and 1998, respectively, a second M.S. degree in transportation safety from George Washington University, Washington, DC, in 2002, and the Ph.D. degree in mechanical engineering from the University of Michigan, Ann Arbor, in 2005.

Currently, he is an Assistant Professor of Mechanical Engineering at Clemson University, Clemson, SC. His current research interests include optimization-based control methods and control of vehicular



**Ilya V. Kolmanovsky** (SM'04) received the M.S. and Ph.D. degrees in aerospace engineering and the M.A. degree in mathematics from the University of Michigan, Ann Arbor, in 1993, 1995, and 1995, respectively.

Currently, he is a Technical Leader at Ford Research Advanced Engineering, Dearborn, MI. In addition to expertise in the automotive powertrain control, his research interests include constrained control, optimization-based control, and control of nonlinear systems. He has served as an Associate Editor

of the IEEE TRANSACTIONS ON CONTROL SYSTEMS TECHNOLOGY (2002–2004) and the IEEE TRANSACTIONS ON AUTOMATIC CONTROL (2005–present).

Dr. Kolmanovsky was a recipient of the 2002 Donald P. Eckman Award of American Automatic Control Council and of the 2002 IEEE TRANSACTIONS ON CONTROL SYSTEMS TECHNOLOGY Outstanding Paper Award.



**Anna G. Stefanopoulou** (SM'05) received the Diploma from the National Technological University of Athens, Greece, in 1991, the M.S. degree in naval architecture and marine engineering, a second M.S. degree in electrical engineering and computer science, and the Ph.D. degree from the University of Michigan, Ann Arbor, in 1992, 1994, and 1996, respectively.

Currently, she is a Professor in the Mechanical Engineering Department at the University of Michigan. She was an Assistant Professor (1998–2000) at the

University of California, Santa Barbara, and a Technical Specialist (1996–1997) at the Scientific Research Laboratories at Ford Motor Company, Dearborn, MI. Her current research interests include control of advanced internal combustion engines and fuel cell power systems.